An off-the-shelf artificial cardiac patch improves cardiac repair after myocardial infarction in rats and pigs

Ke Huang[1,2], **Emily W. Ozpinar**[2,3], **Teng Su**[1,2,3], **Junnan Tang**[1], **Deliang Shen**[1], **Li Qiao**[1], **Shiqi Hu**[1,3], **Zhenhua Li**[1,3], **Hongxia Liang**[1], **Kyle Mathews**[2,4], **Valery Scharf**[4], **Donald O. Freytes**[2,3], **Ke Cheng**[1,2,3,5,*]

[1]Department of Molecular Biomedical Sciences, North Carolina State University, Raleigh, NC 27607, USA.

[2]Comparative Medicine Institute, North Carolina State University, Raleigh, NC 27607, USA.

[3]Joint Department of Biomedical Engineering, University of North Carolina at Chapel Hill and North Carolina State University, Raleigh, NC 27607, USA.

[4]Department of Clinical Sciences, North Carolina State University, Raleigh, NC 27607, USA.

[5]Division of Pharmacoengineering and Molecular Pharmaceutics, Eshelman School of Pharmacy, University of North Carolina at Chapel Hill, Chapel Hill, NC 27599, USA.

Abstract

[*]Corresponding author. ke_cheng@ncsu.edu; ke_cheng@unc.edu.

SUPPLEMENTARY MATERIALS

stm.sciencemag.org/cgi/content/full/12/538/eaat9683/DC1

Materials and Methods

Fig. S1. Characterization of artCP.

Fig. S2. Effects of artCP on endothelial cells in vitro.

Fig. S3. Effects of artCP on CPC differentiation in vitro.

Fig. S4. synCSC retention and biodistribution in rats.

Fig. S5. Immunogenicity of artCP in the post-MI rat heart.

Fig. S6. Rat heart dimensions measured by echocardiography.

Fig. S7. H&E staining of artCP and adjacent myocardium 21 days after transplantation in a rat.

Fig. S8. Treatment effects from empty, cryopreserved, or fresh artCP transplantation in rats.

Fig. S9. Heart morphometric analysis after patch transplantation in rats.

Fig. S10. Liver and kidney functions 21 days after artCP transplantation in rats.

Fig. S11. Percentage of pH3[+] or Ki67^{+} cardiomyocytes in total cells 21 days after patch transplantation in rats.

Fig. S12. Staining of proliferation marker Aurora B after artCP or myoECM transplantation in rats.

Fig. S13. Analyses of myocardial proliferation and apoptosis 21 days after patch transplantation in rats.

Fig. S14. Effects of artCP therapy on angiomyogenesis in rats.

Fig. S15. Cardiac functional assessment of artCP therapy in a porcine MI model.

Fig. S16. Effects of artCP transplantation on liver and kidney functions in the porcine MI model.

Fig. S17. Immunogenicity analysis of artCP transplantation in the porcine MI model.

Table S1. myoECM average tension/stress versus strain.

Table S2. NHT average tension/stress versus strain.

Reference (69)

Competing interests: The authors declare that they have no competing financial interests.

Data and materials availability: All data associated with this study are present in the paper or the Supplementary Materials.

Cell therapy has been a promising strategy for cardiac repair after injury or infarction; however, low retention and engraftment of transplanted cells limit potential therapeutic efficacy. Seeding scaffold material with cells to create cardiac patches that are transplanted onto the surface of the heart can overcome these limitations. However, because patches need to be freshly prepared to maintain cell viability, long-term storage is not feasible and limits clinical applicability. Here, we developed an off-the-shelf therapeutic cardiac patch composed of a decellularized porcine myocardial extracellular matrix scaffold and synthetic cardiac stromal cells (synCSCs) generated by encapsulating secreted factors from isolated human cardiac stromal cells. This fully acellular artificial cardiac patch (artCP) maintained its potency after long-term cryopreservation. In a rat model of acute myocardial infarction, transplantation of the artCP supported cardiac recovery by reducing scarring, promoting angiomyogenesis, and boosting cardiac function. The safety and efficacy of the artCP were further confirmed in a porcine model of myocardial infarction. The artCP is a clinically feasible, easy-to-store, and cell-free alternative to myocardial repair using cell-based cardiac patches.

INTRODUCTION

Coronary heart disease is a leading cause of death in the United States, killing more than 360,000 people a year (1). Current myocardial infarction (MI) treatment approaches, including limiting the initial injury and blocking secondary maladaptive pathways, greatly reduce cardiovascular morbidity and mortality. However, the remodeling process after acute MI still frequently leads to arrhythmias and heart failure and contributes to cardiovascular morbidity and mortality (2). Cell therapies focus on using cells derived from different sources to promote myocardial regeneration by altering the cardiac remodeling process and reducing scar size caused by MI (3–5). Heart-derived cardiac stromal cells (CSCs) offer regenerative therapeutic benefits through secretion of paracrine factors (6–8) and direct interaction with the injured cardiomyocytes (9). Safety and moderate beneficial effects from CSC therapy have been confirmed in clinical trials for patients with mild-moderate MI (10–13).

Clinical applications of cell therapy for heart repair have several limitations (14–16). First, cells are very fragile and have to be carefully preserved to retain viability and functionality before transplantation (17). Consequently, live cells cannot be considered an off-the-shelf product for clinical application. Cell therapy is costly in terms of labor and material expenses. The modes of action for cell therapy products also remain elusive, making it difficult to standardize product release criteria. These issues are further complicated by the fact that some undifferentiated cells can exhibit uncontrolled cell growth or become tumorigenic after transplantation (14, 18). Furthermore, immunogenicity is a concern when allogeneic cells are used. Transplantation of autologous cells offers some advantages (19), but generation of these cells is expensive and time-consuming because each patient's cells represent an independent batch (14). In addition, the extremely low cell retention and engraftment regardless of the delivery route are a major hurdle that hampers the efficacy of cell therapy (20, 21). Such rapid cell loss after transplantation is not mainly due to cell death (22) but rather the "washing away" of the cells from the site of deliver by the actively contracting heart (23–25).

Recently, multiple scaffold materials spiked with stem cells have been engineered to serve as cardiac patches for myocardial regeneration (26–38). However, the aforementioned limitations associated with natural cells remain unsolved for cellular cardiac patches. To overcome these challenges, we designed and fabricated an artificial cardiac patch (artCP) by embedding synthetic CSCs (synCSC) in decellularized myocardial extracellular matrix (ECM) (myoECM). myoECM derived from decellularized porcine myocardium offers an optimal scaffold material, providing native ultrastructural and material properties. myoECM retains bioactivity that has been shown to promote constructive remodeling and vascularization after transplantation (28, 38, 39). synCSCs were fabricated by encapsulating human CSC–secreted factors into biodegradable polylactic-co-glycolic acid (PLGA) microparticles (40, 41). When combined, the three-dimensional (3D) reticulate structure of myoECM offers mechanical support (42) to the native myocardium, whereas the embedded synCSCs secrete regenerative factors. Both components are acellular, overcoming the shortages of using live cells and providing an off-the-shelf product with an extended shelf life (Fig. 1A). Here, we tested the mechanical and biological properties and cryostability of the artCP in vitro and determined its therapeutic benefits in rodent and porcine models of MI. By exploiting cell and ECM biology, the artCP offers an acellular, clinically feasible, off-the-shelf potential therapeutic for cardiac repair.

RESULTS

Fabrication and characterization of artCP

myoECM was derived from decellularized porcine myocardium to function as the basal material for the artCP. To test whether the myoECM had appropriate structure and mechanical characteristics for heart transplantation, we compared myoECM with native porcine heart tissue (NHT) via histology and mechanical testing (Fig. 1, B to F). The results indicated that myoECM was produced efficiently by decellularization, and the remaining fibrillar collagen provided mechanical stability, structural support, and retained tissue morphology (Fig. 1B). The compliance of myoECM was similar to that of NHT with a similar thickness (Fig. 1, C to E). Decellularization effectively removed DNA (Fig. 1F). These results confirmed that decellularized myoECM preserved its reticular structure and maintained a relatively similar elasticity as NHT, rendering a mechanically feasible scaffold for heart transplantation.

To fabricate the final artCP product, we embedded synCSCs (fig. S1A) into myoECM via a vacuum filtration process (Fig. 2A). The vacuum force drove the synCSC particles into the myoECM structure. To confirm synCSC embedding efficiency and retention, artCPs were fluorescently labeled, washed three times with phosphate buffered saline (PBS), and then subjected to microscopic observation. synCSCs remained in the artCP after washing (Fig. 2, B and C). Scanning electron microscope (SEM) confirmed that synCSCs were efficiently embedded in the reticulate structure of myoECM with negligible structural changes (Fig. 2D). Confocal imaging further confirmed that synCSCs were successfully embedded into myoECM and uniformly distributed (fig. S1B). In the presence of collagenase, the artCP degraded (fig. S1C). Together, vacuum filtration was able to embed synCSCs into myoECM

to form the artCP without damaging the structural integrity of either the myoECM or synCSCs.

Cryostability of artCP

One major advantage of an artCP over a cardiac patch containing live cells is its foreseeable cryostability. CSCs rely on secretion of factors to exert their regenerative potency (13). We assessed the concentrations of three regenerative factors [vascular endothelial growth factor (VEGF), hepatocyte growth factor (HGF), and insulin-like growth factor (IGF)] released by artCPs that had been cryostored for various time periods (Fig. 3A). After cryostorage, artCPs were rinsed three times with sterile PBS and soaked in 1 ml of sterile PBS for a 4-day incubation period at 37°C (Fig. 3A). The results indicate that the factor-releasing ability of the artCP was not affected by cryostorage (Fig. 3, B to D). As a quality control, we confirmed that the initial total protein amounts in the synCSCs of different batches of artCPs were similar (Fig. 3E). In addition, we further evaluated the mechanical properties of cryostored and freshly fabricated artCPs. Results indicate that 28 days of cryostorage did not affect the mechanical properties of the patch (fig. S1, D to F).

Regenerative potency of artCP in vitro

As an in vitro potency assay, we incubated fresh or cryopreserved artCPs with neonatal rat cardiomyocytes (NRCMs) for 3 days and assessed cell viability and proliferation. Equal amounts of synCSCs, myoECM, or empty artCP (myoECM embedded with empty PLGA particles without CSC factors) were included as controls. NRCMs cultured in media were used as a negative control. Proliferating NRCMs were identified by Ki67$^+$ expression (Fig. 4A). Our data suggested that incubation with synCSCs, cryopreserved artCP, or fresh artCP promoted NRCM proliferation (Fig. 4B). Coincubation with synCSCs, cryopreserved artCP, or fresh artCP increased cell viability and decreased cell death, resulting in an increase in overall cell numbers (Fig. 4, C and D). Terminal deoxynucleotidyl transferase–mediated deoxyuridine triphosphate nick end labeling (TUNEL) assay revealed that coculture inhibited cell apoptosis (Fig. 4, E and F), and artCP promoted tube formation of endothelial cells (fig. S2, A to C). We also used human-induced pluripotent stem cell (iPSC)–derived cardiac progenitor cells (CPCs) to assess the effects of artCP on cardiac differentiation using cardiac troponin T (cTnT) expression as an indicator. Comparing to CPCs that were treated with the Wnt inhibitor XAV939 (positive control) and CPCs cultured with basal media (negative control), culture with synCSCs or artCP encouraged the differentiation of CPCs (fig. S3, A and B). In all assays, the potency of cryostored artCPs was similar to that of fresh artCPs. Together, these data support that artCPs retain the regenerative potency of synCSCs regardless of cryostorage.

Biodistribution of synCSCs and biocompatibility of artCPs

For biodistribution studies, we induced acute MI by left anterior descending artery (LAD) ligation [as previously described; (43–46)] in Sprague-Dawley (SD) rats. After LAD ligation was confirmed by color alteration of the left ventricle (LV), a circular piece of artCP (diameter = 5 mm) containing ~2×10^6 synCSCs was sutured onto the MI area. We compared application of labeled artCP to myoECM and intramyocardial injection of labeled synCSCs. Twenty-four hours after treatment, all groups of animals were euthanized, and

major organs were collected for ex vivo fluorescence imaging. artCP effectively retained synCSCs within the infarcted region with minimal off-target loss into other organs (fig. S4, A to C). Intramyocardially injected synCSCs were "washed away" from the heart to other organs such as the lungs (fig. S4C). These results were consistent with our previous study (40). The off-target lung distribution was due to vessel damage caused by needle injection and subsequent venous drainage (43). To evaluate the biocompatibility of artCPs, we performed an independent experiment by transplanting artCPs onto post-infarct hearts of SD rats. The hearts were harvested for analysis of immune rejection 7 (fig. S5, A to C) and 21 (fig. S5D) days after transplantation. T cell and macrophage infiltration was evaluated with CD3/CD8 and CD68 staining, respectively. artCP transplantation elicited negligible T cell or macrophage infiltration as only few CD3$^+$ and/or CD8$^+$ T cells, and CD68$^+$ macrophages were detected in the hearts.

artCP therapy in rats with acute MI

To test the therapeutic potency of artCP, we induced MI in SD rats and sutured a circular piece of artCP (diameter = 5 mm) containing $\sim 2 \times 10^6$ synCSCs onto the MI area. Rats in the empty myoECM control treatment group received an empty myoECM patch (diameter = 5 mm) without synCSCs. Negative control animals did not receive any treatment after MI. All animals were euthanized 21 days after the surgery, and hearts were harvested for histological analysis (Fig. 5A). The surgeon and the analyzer were blinded to the treatment groups. Echocardiography was performed before MI induction, 4 hours after the operation (injury baseline), and before the animals were euthanized on day 21 (end point) (Fig. 5B). Left ventricular ejection fraction (LVEF) and left ventricular fractional shortening (LVFS) before surgery and 4 hours after surgery were indistinguishable among all three groups (Fig. 5, C and D), indicating uniform cardiac function and degree of initial injury. Three weeks after treatment, the hearts that had received artCP transplantation had the greatest LVEFs (Fig. 5, E and F), LVFSs (Fig. 5, G to J), and cardiac contractility (fig. S6). Hematoxylin and eosin (H&E) staining revealed the structures of artCP and myoECM 3 weeks after transplantation (Fig. 6A). According to morphology, cells residing in the structures were likely fibro-blasts, smooth muscle cells, and endothelial cells (fig. S7). Masson's trichrome staining (Fig. 6B) indicated that artCP transplantation promoted reduction in infarct size (Fig. 6C), increase in viable tissue in the risk area (Fig. 6D), and increase in LV wall thickness (Fig. 6E). A large amount of viable cardiac tissue in the infarcted region was covered by the artCP (Fig. 6, A and B). Consistent with previous studies (39, 44), empty myoECM transplantation also generated some therapeutic effects; however, the embedding of synCSCs in the artCP further amplified the therapeutic benefits.

artCP's therapeutic effects are not affected by cryostorage

We performed a separate animal study to compare the therapeutic potency of cryopreserved artCPs to their freshly made counterparts. Immediately after MI induction, rats received fresh or cryopreserved artCPs (cryostored for 28 days at −80°C). Animals receiving MI without treatment or treatment of empty artCP (no synCSCs) were used as controls. LVEFs and LVFSs were determined before MI, 4 hours after MI, and 3 weeks after MI (fig. S8, A to P). The LVEFs and LVFSs before MI and 4 hours after MI were indistinguishable among groups, indicating a similar degree of initial injury (fig. S8, A and B). Twenty-eight days of

cryostorage did not affect the artCP's ability to protect cardiac function (fig. S8, A to P). In addition, infarct sizes were reduced to a similar degree by treatment with cryopreserved or fresh artCP (fig. S9, A and B). Viable tissue in the risk area (fig. S9C) and infarct wall thickness (fig. S9D) were increased by both therapies. These results demonstrated the cryostability of artCP products. On day 21, the serum concentrations of alanine aminotransferase (ALT), aspartate aminotransferase (AST), creatinine, and blood urea nitrogen (BUN) (fig. S10) were indistinguishable among all groups, indicating no toxicity from artCP transplantation.

artCP therapy promotes angiomyogenesis in rats with MI

ArtCP transplantation increased capillary density in the infarct area (Fig. 7, A and B). To further explore whether cardiac functional improvement was accompanied by myocardial repair, we stained tissue sections with three cell cycling markers [Ki67, phosphorylated histone H3 (pH3), and Aurora B kinase (Aurora B)]. The myocyte and nonmyocyte localizations of these markers were confirmed by z-stack confocal imaging (Fig. 7, C to G). Results indicate that Ki67$^+$ and pH3$^+$expressions in artCP-treated hearts overlaid with cardiomyocyte nuclei (fig. S11). Aurora B$^+$ (fig. S12, A and B) staining confirmed the ability of artCP and myoECM therapy to promote cell proliferation. TUNEL assay indicated that artCP transplantation decreased cell apoptosis in the infarct border zone (fig. S13, A and B). The proregenerative and antiapoptotic mechanisms of artCP therapy were further confirmed by Western blot analysis (fig. S13, C to F). Moreover, fresh or cryopreserved artCP therapy promoted angiomyogenesis to a greater extent than application of empty artCP (fig. S14, A to G). Together, transplantation of artCPs strengthened angiomyogenesis while reducing cell apoptosis.

artCP therapy in a porcine model of MI

A porcine model has been used widely as a translational tool in cardiovascular research because pigs have similar cardiac anatomy to humans (45). A porcine MI model was created in Yorkshire pigs (female, 20 to 30 kg) by open-chest surgery and LAD ligation distal to the second diagonal branch (Fig. 8A). A piece of artCP (diameter = 3.5 cm) was transplanted onto the surface of the porcine heart to cover the MI area. Control animals did not receive any treatment. All animals were euthanized 7 days after treatment, and the hearts were harvested for morphometry and histology studies. Blood samples and electrocardiograms (ECGs) were collected before MI, 24 hours, and 7 days after MI. Induction of MI was verified by the elevation of ST segment on ECG and increased serum cardiac troponin I concentration 24 hours after MI (Fig. 8, B and C). Control animals still had ST segment elevation at day 7, whereas this abnormality disappeared in the artCP-treated animals (Fig. 8B). After the last echocardiography session, animals were euthanized, and all hearts were collected and cryosectioned transversally (1 cm in thickness) from apex to level of ligation for triphenyl tetrazolium chloride (TTC) staining. The infarct size in each slice was quantified by ImageJ analysis. Macroscopic images from TTC staining suggested that the infarcted area of artCP-transplanted hearts was significantly smaller on slice 2 (P = 0.0158; Fig. 8, D and E). Masson's trichrome staining revealed that artCP treatment reduced myocardial fibrosis at the microscopic level qualitatively (Fig. 8F).

Echocardiography data were collected at 24 hours (baseline) and 7 days after MI (end point) for cardiac function analysis (fig. S15, A to H). Results show that artCP treatment improved cardiac function (measured by LVEF) and cardiac contractility (measured by LVFS). To assess the safety of artCP transplantation, we evaluated liver and kidney toxicity of artCP using blood samples from before MI, 24 hours after MI, and 7 days after MI. The concentration of ALT and AST was indistinguishable among groups (fig. S16, A and B), indicating that artCP transplantation did not lead to hepatic damage. Furthermore, blood creatinine and BUN measurements indicated that artCP transplantation did not generate kidney injury (fig. S16, C and D). To address the potential immune reaction against the artCP, we quantified white blood cells, polymorphonuclear leukocytes, and lymphocytes. No changes were detected in the artCP-treated animals over 7 days after MI (fig. S17, A to D). Compared to untreated animals, reactive lymphocytes in artCP-treated animals were suppressed 24 hours after MI (fig. S17D). These results further support that artCP is biocompatible and safe in the porcine model.

DISCUSSION

As emerging strategies in tissue engineering and regenerative medicine, cardiac patches (26, 46, 47) and cell therapy (13, 48–50) have become the focus of studies targeting myocardial tissue repair during the past decade. A cardiac patch is typically created by spiking a scaffold material with stem cells (50–54). In general, these patches rely on the added cells to impart functional benefits to injured tissue. However, as a living component, the cells also make the cardiac patch product vulnerable to ambient storage and shipping conditions (14). Therefore, methods to generate therapeutic cardiac patches that are stable at room temperature and offer ready-to-use convenience remain of interest. Recent development in synthetic strategies provides alternatives to patches that incorporate living cells (40, 41, 54–56). Here, we embedded therapeutic synCSCs within decellularized myoECM to generate a fully acellular artCP. The artCP approach adopts a "particle in matrix" design harnessing the proven beneficial effects of synCSCs and myoECM: The synCSCs mimick the therapeutic features of live stem cells while overcoming their storage and survival problems, and the myoECM preserves the ECM structures and bioactivity found within native cardiac tissue.

We confirmed the stability and therapeutic potency of artCPs after 28 days of cryostorage. If not stored and handled properly, then traditional cardiac patches (with live stem cells) would suffer from cell death within the patch and subsequent negative effects or lack of therapeutic efficacy after transplantation. Our cryopreserved artCPs retained potency as assessed by in vitro culture with rodent myocytes. The myoECM in the artCP supports the cardiac retention of synCSCs upon application to the heart, whereas the synCSCs release proregenerative factors. In our previous work, synCSCs were directly injected into the myocardium (40). Despite encouraging proof-of-concept results, this delivery strategy was insufficient: synCSCs accumulated in the lungs, distant from the site of injection. This finding was confirmed in the present study. In contrast, the artCP approach reinforced the retention of synCSCs on the heart and diminished their off-target biodistribution to other organs. In both rodent and porcine models of MI, we demonstrated that transplantation of artCPs improved heart pump function, reduced fibrosis/infarct size, increased viable myocardial tissue, and promoted angiomyogenesis.

Our study has several limitations. As a pilot study, the sample size of the pig study is small. However, the observations are in line with those results from rodent studies, which were sufficiently powered. Future large animal studies with larger sample sizes and longer follow-up duration are needed before clinical translation. For tracking long-term heart infarct size changes in large animals, magnetic resonance imaging would be an ideal tool due to its noninvasive nature and reliability. In addition, to reduce the injury associated with open-chest surgery, minimally invasive approaches of patch delivery need to be developed in future iterations (55, 57–59). A recent study showed that intracardiac injection of two types of adult stem cells can stimulate recruitment and activation of $CCR2^+$ and $CX3CR1^+$ macrophages, which then rejuvenate the injured heart via modulating cardiac fibroblast activities (60). Although we detected $Ki67^+$ and $pH3^+$ cardiomyocytes in the infarcted area after artCP treatment, the full extent of proliferation induced by the artCP remains to be determined. Further mechanistic studies on myocardial regenerative pathways (61–63) and tracing the origin of proliferating cardiomyocytes could help elucidate the modes of action of artCP therapies. Furthermore, the duration of factor release and artCP degradation in vivo need to be optimized to match the post-MI LV remodeling. Nevertheless, the present study shows the potential therapeutic effects of using synCSCs with myoECM in an acellular cardiac patch for myocardial regeneration.

MATERIALS AND METHODS

Study design

The purpose of this study was to design an off-the-shelf artCP for myocardial repair after infarction to overcome the limitations of using living stem cells. The artCP was fabricated by embedding PLGA-encapsulated factors secreted from human CSCs (synCSCs) into a decellularized porcine myocardial scaffold (myoECM). In vitro, we performed studies to determine the 3D structure, mechanical properties, cryostability, degradation, and therapeutic potency of artCPs. In vivo, rat models of MI were used to determine the safety and efficacy of artCP therapy. In addition, a pilot porcine study was used to confirm the results from rodent studies. We compared cryopreserved and freshly prepared artCPs in vitro and in vivo (rat studies) to assess patch cryostability. Animals were randomized to treatment groups. Cardiac function measurement and histological analysis were performed in blinded fashions. All animal work was compliant with the Institutional Animal Care and Use Committee at the North Carolina State University.

Preparation of conditioned media

Conditioned media from human CSCs were prepared as previously described (40, 64). Briefly, 2×10^6 human CSCs from nine cell lines that derived from primary cells in-house were cultured in T-75 flasks with 15 ml of 20% fetal bovine serum (FBS) media in 5% CO_2 at 37°C. When cells reached 80% confluency, cells were rinsed with 10 ml of FBS-free media once per 30 min for 12 times in total. Then, cells were incubated in 15 ml of FBS-free media for 14 days in 5% CO_2 at 37°C without media change. The media were collected and centrifuged at $1000g$ for 10 min to remove the cells and large fragments. To diminish the variable batch quality, conditioned media from nine cell lines were mixed before lyophilization and storage. For additional details, see the Supplementary Materials.

Fabrication of synCSCs

Conditioned media contain growth factors secreted by CSCs. As a biocompatible and biodegradable polymer, PLGA has provided a safe and nontoxic building block for various controlled release systems. synCSCs were fabricated according to previously described polymer encapsulation approaches (40). Briefly, we fabricated CSC factor–loaded synCSCs by a water/oil/water (w/o/w) emulsion technique. We mixed human CSC–conditioned media containing polyvinyl alcohol (PVA) (0.1%, w/v) as the internal aqueous phase in methylene chloride (DCM) containing PLGA as the oil phase. The mixture was sonicated on ice for 30 s and immediately introduced into water with PVA (0.7%, w/v) to produce a w/o/w emulsion. The secondary emulsion was emulsified for 5 min on a high-speed homogenizer. The w/o/w emulsion was continuously stirred overnight at room temperature to promote solvent evaporation. The solidified synCSCs were centrifuged, washed with sterilize PBS, lyophilized, and stored at −80°C. Varying the volumetric ratio of w/o/w and the amount of PLGA in the oil phase produces PLGA microparticles with different sizes and shell thicknesses.

Preparation of myoECM

Porcine hearts were decellularized as previously described (42). Briefly, whole hearts of market-weight pigs were obtained from the Nahunta Pork Center. Heart tissue was cleaned of excess nonmyocardial tissue and washed thoroughly with tap water. The tissues were then patted dry and placed at −80°C for at least 48 hours. The heart was sliced into 1-mm thin pieces and agitated in a series of washes. The tissues were first rinsed with deionized water and washed twice with PBS before washing for 2 hours in 0.05% trypsin (Thermo Fisher Scientific), 2 hours in 2% Tween 20 (Sigma-Aldrich), and 2 hours in 4% sodium deoxycholate solution (Sigma-Aldrich). Five-minute deionized water and two 15-min PBS washes were performed between the trypsin, Tween 20, and sodium deoxycholate steps. The heart slices were then sterilized with a 0.1% peracetic acid solution (Sigma-Aldrich) and washed three times with sterile 1× PBS. Decellularized myoECM was then placed flat on aluminum foil and lyophilized for at least 24 hours. Lyophilized myoECM scaffolds were then sterilized using ethylene oxide.

DNA quantification of myoECM

Samples of heart tissue (~10 mg) were taken before and after decellularization and were digested at 60°C overnight with papain (0.2 mg/ml; Sigma-Aldrich). The samples were then analyzed for DNA content using the Quant-IT Picogreen dsDNA Assay (Thermo Fisher Scientific, Waltham, MA) according to the manufacturer's instructions. Samples (100 μl) were read at 538 nm with an excitation at 485 nm using a fluorescence spectrometer. Before decellularization, samples contained 418.8 ± 27.33 ng of DNA/mg of tissue ($n = 8$), and after decellularization, samples contained 17.66 ± 3.869 ng of DNA/mg of tissue ($n = 8$).

Characterization of myoECM

Biopsy punches (7 mm) were taken of the heart tissue before and after decellularization, fixed with 4% paraformaldehyde (Sigma-Aldrich) overnight, and stored in 70% EtOH. Cross sections were cut at 5 μm and stained for Van Gieson's, Gömöri's trichrome, and Alcian

blue. Slides were imaged using an AZ100 multipurpose zoom microscope system. Mechanical testing was done on an Instron 5944 with a 50 N load cell. Samples of myocardium were randomly cut into rectangular pieces, hydrated in $1\times$ PBS until testing, and then secured at opposite ends onto customized clamps. Samples of NHT were 12.62 ± 0.60 mm in width and 1.79 ± 0.13 mm for $n = 5$ in thickness. Processed myoECM samples were 10.05 ± 0.59 mm in width (9.47 ± 0.60 mm for $n = 5$) and (1.54 ± 0.13 mm for $n = 5$) in thickness. Samples were preconditioned using five cycles at a rate of 1% strain/s with a preload of 0.06 N. This was followed by a uniaxial stretch of until failure at a rate of 1% strain/s. Data were collected using Bluehill 3 Testing Software and processed.

Fabrication and characterization of artCPs

myoECM (diameter = 3.5 cm) was hydrolyzed with sterilized PBS for 24 hours and then placed on the filtration area of the 50-ml vacuum filtration system (Steriflip filter units). synCSCs suspended in sterilized PBS (7×10^6/ml) were added evenly on top of the myoECM so that the vacuum extraction force drove the synCSCs into the reticulate structure of myoECM during vacuum filtration and formed artCP. The artCP was cut into round pieces (diameter = 5 mm) with a size 10 scalpel for both in vitro study and in vivo rat study. The artCP for the in vivo porcine study was a round piece with a diameter of 3.5 cm. The morphology of artCP was studied by SEM (Philips XL30 scanning microscope, Philips). Freeze-dried samples were mounted on aluminum stubs with double-sided tape and coated with a thin layer of gold. The coated samples were then scanned and photographed under the microscope at an acceleration voltage of 15 kV. To examine the embedding efficiency and retention of synCSCs in vitro, we prelabeled myoECM with anti–collagen I (1:100; ab34710, Abcam) and fluorescein isothiocyanate (FITC)–conjugated secondary antibodies (1:200). Also, we prelabeled synCSCs with red fluorescent Texas Red succinimidyl ester (1 mg/ml; Invitrogen). Then, the artCP ($n = 6$) was produced for imaging before and after sterilized PBS wash. Images were taken with an epifluorescence microscope (Olympus IX81). The retained synCSCs were characterized and compared from the same images using the National Institutes of Health (NIH) ImageJ software.

Cryostability analysis of artCPs

We created five batches ($n = 4$ in each batch) of artCP every 7 days. For the first four batches, the artCPs were washed with PBS and cryostored in −20°C directly after fabrication. On day 28, the first four batches were thawed, and the fifth batch of artCP was freshly made. Then, we rinsed all batches of artCP with sterile PBS three times and soaked in 1 ml of sterile PBS. After that, we incubated artCPs in a 37°C incubator for 4 days. Regenerative factors (VEGF, HGF, and IGF) in the supernatant were assessed through enzyme linked immunosorbent assay (ELISA) kits (R&D Systems). Total protein content of synCSCs used for artCP batch creation was determined as in previous studies (40). Briefly, 10 mg of freeze-dried synCSCs was dissolved in 1 ml of DCM for 60 min. Then, 1 ml of PBS was added into solution followed by agitation for 10 min to extract protein from DCM into PBS. After centrifugation, the concentration of protein in the aqueous phase was determined by the BCA (bicinchoninic acid) Protein Assay Kit (Thermo Fisher Scientific).

In vitro potency of artCPs

NRCMs were derived from SD rats as previously described (65). We cultured NRCMs on four-well chamber slides. Small pieces (1 mm^2) of fresh artCP, cryopreserved artCP, myoECM, or 1.2 μl of synCSC solution (7×10^6/ml; synCSCs suspended in sterilized PBS) were added into NRCM culture chamber for 3 days. An NRCM culture without any additions to the media (standard culture conditions) was included as a control. Cell proliferation was evaluated by the percentage of sarcomeric α-actinin–positive (α-SA$^+$) (1:100; a7811, Sigma-Aldrich)/Ki67$^+$ (1:100; ab15580, Abcam) NRCMs. For assessment of cell apoptosis, the cells were incubated with TUNEL solution (Roche Diagnostics GmbH) and counterstained with 4′,6-diamidino-2-phenylindole (DAPI) (Life Technologies, NY, USA). A LIVE/DEAD Viability/Cytotoxicity Kit (Thermo Fisher Scientific) was used to determine the cell viability of NRCMs. Images were taken with a confocal fluorescence microscope (ZEISS LSM 880). Tissue morphology was characterized by images using the NIH ImageJ software and ZEN lite software.

Angiogenesis assay

Human umbilical vein endothelial cells (American Type Culture Collection, PCS-100–010) were coincubated with PBS, small pieces (1 mm^2) of myoECM, cryopreserved artCP, or freshly prepared artCP for 24 hours and then plated on growth factor–deprived Matrigel (BD Biosciences) to evaluate angiogenesis (66). Eight hours later, tube formation was measured with a white light microscope and analyzed with NIH ImageJ software.

Differentiation assay

Human iPSC–derived cardiac progenitor cells (iCell Cardiac Progenitor Cells, Fujifilm Cellular Dynamics) were used as an in vitro cellular model to evaluate the effects of artCP on cardiac differentiation (67). Briefly, CPCs were cultured with XAV939/SB431542 (positive control)–, synCSC-, myoECM-, or artCP-containing maintenance medium for 2 days and then switched to maintenance medium for 4 to 6 days. Negative control was CPCs cultured with maintenance medium for 7 days. Immunohistochemistry (IHC) for cTnT was performed. Images were taken with a confocal fluorescence microscope (ZEISS LSM 880). Tissue morphology was characterized using the NIH ImageJ software and ZEN lite software. Also, cells in each group were fixed in 2% paraformaldehyde for 30 min at room temperature and permeabilized and blocked in flow buffer for 1 hour. Cells were incubated with mouse anti-cTnT antibody (1:400; Thermo Fisher Scientific) for 1 hour at 4°C and then incubated with anti-mouse Alexa Fluor 488 antibodies for 30 min. The samples were analyzed using flow cytometry (CytoFlex flow cytometer, Beckman Coulter). Data analysis was processed with the FlowJo software.

Rat model of MI

Five- to 7-week-old female SD rats (Charles River Laboratories) were anesthetized with a 1.5% isoflurane-oxygen mixture before intraperitoneal administration of anesthetic combination (0.8 to 0.9 μl/g; ketamine and xylazine with a proportion of 2:1). Under artificial ventilation with a rodent ventilator (SAR-1000 Small Animal Ventilator), MI was induced under sterile surgical conditions. Briefly, the heart was exposed by left thoracotomy

at the fourth intercostal space, and acute MI was produced by permanent ligation of LAD (6–0 prolene, eSutures). Then, the rats were left in situ for 20 min [open chest covered with a sterile PBS-soaked cotton gauze pad (Fisherbrand)]. The heart was randomized to receive one of the following three treatments: (i) MI induction without any treatment (MI group), (ii) MI induction with application of empty myoECM patch sutured onto the surface of the discolored infarcted area (MI + myoECM group), or (iii) MI induction with artCP sutured onto the surface of discolored infarcted area (MI + artCP group). After chest closure and completion of surgery, rats were extubated and observed for about 30 min until they were able to move. Twenty-one days (rat 21 days is equal to human 1.5 years) (68) after MI, the animals were euthanized for further study.

Immunohistochemistry

Heart cryosections were fixed with 4% paraformaldehyde solution, permeabilized and blocked with 0.01% saponin (Sigma-Aldrich) Dako solution, and then incubated with primary antibodies overnight at 4°C: mouse anti–α-SA (1:100; a7811, Sigma), rabbit anti-Ki67 (1:100; ab15580, Abcam), rabbit anti–von Willebrand factor (1:100; ab6994, Abcam), rabbit anti- pH3 (1:100; ab5176, Abcam), rabbit anti–Aurora B (1:100; ab2254, Abcam). FITC- or Texas Red secondary antibodies (1:200) were obtained from Abcam Company and used with these primary antibodies for 1.5 hour at room temperature. Samples were then treated with DAPI (Life Technologies) and mounted in Prolong Gold Mounting Media (Life Technologies). For assessment of cell apoptosis, heart cryo-sections were incubated with TUNEL solution (Roche Diagnostics GmbH) and counter-stained with DAPI (Life Technologies). Images were taken with an epifluorescent microscope (Olympus IX81) and confocal fluorescent microscope (ZEISS LSM 880). Tissue morphology was characterized from the images using the NIH ImageJ software and ZEN lite software.

Immunogenicity detection after artCP transplantation

SD rats with intact immune systems were anaesthetized with ketamine and xylazine cocktail (proportion of 2:1). Under sterile conditions, the heart was infarcted by LAD ligation. ArtCP was transplanted onto the heart (6–0 prolene, eSutures). After 7 days, all rats were sacrificed, and hearts were collected for cryosections as previously described. IHC was performed with primary antibodies including rabbit anti-CD3 (1:100; ab16669, Abcam), mouse anti-CD8 alpha (1:100; mca48r, AbD Serotec), and mouse anti-CD68 (1:100; ab955, Abcam). FITC-conjugated secondary antibodies (1:200) were obtained from Abcam Company and used with these primary antibodies. Nuclei were stained with DAPI (Life Technology). Images were taken by an Olympus epifluorescence microscopy system.

synCSC retention and distribution in vivo

To track the synCSCs in vivo, we fabricated artCPs with DiR (1,1-dioctadecyl-3,3,3,3-tetramethy-lindotricarbocyanine iodide)–labeled synCSC and transplanted them in rat MI models. To prepare DiR (D12731, Invitrogen, Life Technologies)–labeled synCSC, the filtered CSC membrane was collected as previously described (40) and was incubated with 1 μM fluorescent lipophilic tracer DiR at room temperature for 20 min. Then, we cloaked the synCSC with DiR-labeled CSC membrane so that the DiR fluorescence could be traced. The animals received intramyocardial injection of DiR-labeled synCSCs ($n = 3$) or

transplantation of empty myoECM as controls ($n = 3$). Animals were euthanized, and organs were harvested 24 hours after treatment. We placed hearts and other organs in the Xenogen IVIS Imaging System (Caliper Life Sciences) to detect red fluorescent protein fluorescence for biodistribution analysis.

artCP transplantation in a porcine MI model

Yorkshire pigs (20 to 30 kg) were used for surgical (open-chest) MI models. While porcine were in their quarters, they were sedated with TKX cocktail [Telazol, a commercially available combination of tiletamine and zolazepam, rehydrated with 2.5 ml each of ketamine (100 mg/ml) and xylazine (100 mg/ml) yielding a final concentration of 50 mg/ml of each of the four components, 1 ml/13 to 30 kg, intramuscularly]. Animals were intubated, and anesthesia was maintained with a mixture of isoflurane (0 to 5% in 100% oxygen) at the constant rate infusion of 5 to 10 μg/kg per hour. While under anesthesia, the pigs were monitored per veterinary hospital guidelines. A partial midline sternotomy was performed under sterile conditions, and the pericardium was sectioned. MI was created by permanent ligation (4–0 prolene, B. Braun Suture) at the distal LAD artery after the second diagonal branch. Heparin (5000 IU, intravenously) was administered just before LAD occlusion. Ten minutes later, the artCP was transplanted by suturing (4–0 prolene, eSutures) on the heart surface downstream of the LAD, where there was a sign of ischemia (discoloration of tissue). During surgery, positive pressure ventilation was maintained at a rate of 10 to 12 breaths/min, and normal saline (10 ml/kg/hour) was infused through the venous cannula in the auricular vein to maintain preload stability. After the study, arterial oxygen tension, locomotor activity, respiratory changes, body temperature, and food and water intake were closely monitored by veterinary services staff. Pigs were followed until 7 days after MI surgery.

Statistical analysis

All results are expressed as means ± SD. Comparison between two groups was performed with two-tailed Student's t test. Comparisons among more than two groups were performed using one-way analysis of variance (ANOVA) followed by post hoc Bonferroni test. Differences were considered statistically significant when $P < 0.05$. Auxiliary supplementary data are provided in tables S1 and S2.

Supplementary Material

Refer to Web version on PubMed Central for supplementary material.

Funding:

REFERENCES AND NOTES

1. Benjamin EJ, Blaha MJ, Chiuve SE, Cushman M, Das SR, Deo R, de Ferranti SD, Floyd J, Fornage M, Gillespie C, Isasi CR, Jiménez MC, Jordan LC, Judd SE, Lackland D, Lichtman JH, Lisabeth L,

Liu S, Longenecker CT, MacKey RH, Matsushita K, Mozaffarian D, Mussolino ME, Nasir K, Neumar RW, Palaniappan L, Pandey DK, Thiagarajan RR, Reeves MJ, Ritchey M, Rodriguez CJ, Roth GA, Rosamond WD, Sasson C, Towfghi A, Tsao CW, Turner MB, Virani SS, Voeks JH, Willey JZ, Wilkins JT, Wu JHY, Alger HM, Wong SS, Muntner P, Heart disease and stroke statistics —2017 update: A report from the American Heart Association. Circulation 135, e146–e603 (2017). [PubMed: 28122885]

2. Swynghedauw B, Molecular mechanisms of myocardial remodeling. Physiol. Rev 79, 215–262 (1999). [PubMed: 9922372]

3. Tompkins BA, Balkan W, Winkler J, Gyöngyösi M, Goliasch G, Fernández-Avilés F, Hare JM, Preclinical studies of stem cell therapy for heart disease. Circ. Res 122, 1006–1020 (2018). [PubMed: 29599277]

4. Duelen R, Sampaolesi M, Stem cell technology in cardiac regeneration: A pluripotent stem cell promise. EBioMedicine 16, 30–40 (2017). [PubMed: 28169191]

5. Matsa E, Burridge PW, Wu JC, Human stem cells for modeling heart disease and for drug discovery. Sci. Transl. Med 6, 239ps6 (2014).

6. Hodgkinson CP, Bareja A, Gomez JA, Dzau VJ, Emerging concepts in paracrine mechanisms in regenerative cardiovascular medicine and biology. Circ. Res 118, 95–107 (2016). [PubMed: 26837742]

7. Walter J, Ware LB, Matthay MA, Mesenchymal stem cells: Mechanisms of potential therapeutic benefit in ARDS and sepsis. Lancet Respir. Med 2, 1016–1026 (2014). [PubMed: 25465643]

8. Lanzoni G, Oikawa T, Wang Y, Cui C-B, Carpino G, Cardinale V, Gerber D, Gabriel M, Dominguez-Bendala J, Furth ME, Gaudio E, Alvaro D, Inverardi L, Reid LM, Clinical programs of stem cell therapies for liver and pancreas. Stem Cells 31, 2047–2060 (2013). [PubMed: 23873634]

9. Xie Y, Ibrahim A, Cheng K, Wu Z, Liang W, Malliaras K, Sun B, Liu W, Shen D, Cho HC, Li T, Lu L, Lu G, Marbán E, Importance of cell-cell contact in the therapeutic benefits of cardiosphere-derived cells. Stem Cells 32, 2397–2406 (2014). [PubMed: 24802280]

10. Makkar RR, Smith RR, Cheng K, Malliaras K, Thomson LEJ, Berman D, Czer LSC, Marbán L, Mendizabal A, Johnston PV, Russell SD, Schuleri KH, Lardo AC, Gerstenblith G, Marbán E, Intracoronary cardiosphere-derived cells for heart regeneration after myocardial infarction (CADUCEUS): A prospective, randomised phase 1 trial. Lancet 379, 895–904 (2012). [PubMed: 22336189]

11. Marbán E, A mechanistic roadmap for the clinical application of cardiac cell therapies. Nat. Biomed. Eng 2, 353–361 (2018). [PubMed: 30740264]

12. Malliaras PK, Makkar RR, Smith RR, Cheng K, Wu E, Bonow RO, Marbán L, Mendizabal A, Cingolani E, Johnston PV, Gerstenblith G, Schuleri KH, Lardo AC, Marbán E, Intracoronary cardiosphere-derived cells after myocardial infarction: Evidence of therapeutic regeneration in the final 1-year results of the CADUCEUS trial. J. Am. Coll. Cardiol 63, 110–122 (2014). [PubMed: 24036024]

13. Cheng K, Ibrahim A, Hensley MT, Shen D, Sun B, Middleton R, Liu W, Smith RR, Marbán E, Relative roles of CD90 and c-kit to the regenerative efficacy of cardiosphere-derived cells in humans and in a mouse model of myocardial infarction. J. Am. Heart Assoc 3, e001260 (2014). [PubMed: 25300435]

14. Tang J-N, Cores J, Huang K, Cui X-L, Luo L, Zhang J-Y, Li T-S, Qian L, Cheng K, Concise review: Is cardiac cell therapy dead? Embarrassing trial outcomes and new directions for the future. Stem Cells Transl. Med 7, 354–359 (2018). [PubMed: 29468830]

15. Kruse C, Danner S, Rapoport DH, Current stem cell technology: Limitations and realistic expectations. Eng. Life Sci 8, 13–18 (2008).

16. Lim JM, Lee M, Lee EJ, Gong SP, Lee ST, Stem cell engineering: Limitation, alternatives, and insight. Ann. N. Y. Acad. Sci 1229, 89–98 (2011). [PubMed: 21793843]

17. Strobel J, Brenner L, Zimmermann R, Weiss D, Zingsem J, Eckstein R, Weisbach V, Influence of duration and temperature of transport and storage prior to processing on cell quality of cord blood units--a German. Experience. Clin. Lab 61, 1453–1461 (2015). [PubMed: 26642707]

18. Herberts CA, Kwa MSG, Hermsen HPH, Risk factors in the development of stem cell therapy. J. Transl. Med 9, 29 (2011). [PubMed: 21418664]

19. Chabannon C, Kuball J, Bondanza A, Dazzi F, Pedrazzoli P, Toubert A, Ruggeri A, Fleischhauer K, Bonini C, Hematopoietic stem cell transplantation in its 60s: A platform for cellular therapies. Sci. Transl. Med 10, eaap9630 (2018). [PubMed: 29643233]

20. Zeng L, Hu Q, Wang X, Mansoor A, Lee J, Feygin J, Zhang G, Suntharalingam P, Boozer S, Mhashilkar A, Panetta CJ, Swingen C, Deans R, From AHL, Bache RJ, Verfaillie CM, Zhang J, Bioenergetic and functional consequences of bone marrow–derived multipotent progenitor cell transplantation in hearts with postinfarction left ventricular remodeling. Circulation 115, 1866–1875 (2007). [PubMed: 17389266]

21. Cheng K, Li T-S, Malliaras K, Davis DR, Zhang Y, Marbán E, Magnetic targeting enhances engraftment and functional benefit of iron-labeled cardiosphere-derived cells in myocardial infarction. Circ. Res 106, 1570–1581 (2013).

22. Cambria E, Pasqualini FS, Wolint P, Günter J, Steiger J, Bopp A, Hoerstrup SP, Emmert MY, Translational cardiac stem cell therapy: Advancing from first-generation to next-generation cell types. npj Regen. Med 2, 17 (2017). [PubMed: 29302353]

23. Terrovitis JV, Smith RR, Marbán E, Assessment and optimization of cell engraftment after transplantation into the heart. Cir. Res 106, 479–494 (2010).

24. Blocklet D, Toungouz M, Berkenboom G, Lambermont M, Unger P, Preumont N, Stoupel E, Egrise D, Degaute J-P, Goldman M, Goldman S, Myocardial homing of nonmobilized peripheral-blood CD34$^+$ cells after intracoronary injection. Stem Cells 24, 333–336 (2006). [PubMed: 16223854]

25. Doyle B, Kemp BJ, Chareonthaitawee P, Reed C, Schmeckpeper J, Sorajja P, Russell S, Araoz P, Riederer SJ, Caplice NM, Dynamic tracking during intracoronary injection of ^{18}F-FDG-labeled progenitor cell therapy for acute myocardial infarction. J. Nucl. Med 48, 1708–1714 (2007). [PubMed: 17909258]

26. Jackman CP, Ganapathi AM, Asfour H, Qian Y, Allen BW, Li Y, Bursac N, Engineered cardiac tissue patch maintains structural and electrical properties after epicardial implantation. Biomaterials 159, 48–58 (2018). [PubMed: 29309993]

27. Wang Q, Yang H, Bai A, Jiang W, Li X, Wang X, Mao Y, Lu C, Qian R, Guo F, Ding T, Chen H, Chen S, Zhang J, Liu C, Sun N, Functional engineered human cardiac patches prepared from nature's platform improve heart function after acute myocardial infarction. Biomaterials 105, 52–65 (2016). [PubMed: 27509303]

28. Bejleri D, Streeter BW, Nachlas ALY, Brown ME, Gaetani R, Christman KL, Davis ME, A bioprinted cardiac patch composed of cardiac-specific extracellular matrix and progenitor cells for heart repair. Adv. Healthc. Mater 7, e1800672 (2018). [PubMed: 30379414]

29. Gao L, Kupfer ME, Jung J, Yang L, Zhang P, Sie YD, Tran Q, Ajeti V, Freeman BT, Fast VG, Campagnola PJ, Ogle BM, Zhang J, Myocardial tissue engineering with cells derived from human induced-pluripotent stem cells and a native-like, high-resolution, 3-dimensionally printed scaffold. Circ. Res 120, 1318–1325 (2017). [PubMed: 28069694]

30. Weinberger F, Breckwoldt K, Pecha S, Kelly A, Geertz B, Starbatty J, Yorgan T, Cheng K-H, Lessmann K, Stolen T, Scherrer-Crosbie M, Smith G, Reichenspurner H, Hansen A, Eschenhagen T, Cardiac repair in guinea pigs with human engineered heart tissue from induced pluripotent stem cells. Sci. Transl. Med 8, 363ra148 (2016).

31. Schaefer JA, Guzman PA, Riemenschneider SB, Kamp TJ, Tranquillo RT, A cardiac patch from aligned microvessel and cardiomyocyte patches. J. Tissue Eng. Regen. Med 12, 546–556 (2018). [PubMed: 28875579]

32. Su T, Huang K, Daniele MA, Hensley MT, Young AT, Tang J, Allen TA, Vandergriff AC, Erb PD, Ligler FS, Cheng K, Cardiac stem cell patch integrated with microengineered blood vessels promotes cardiomyocyte proliferation and neovascularization after acute myocardial infarction. ACS Appl. Mater. Interfaces 10, 33088–33096 (2018). [PubMed: 30188113]

33. Feiner R, Engel L, Fleischer S, Malki M, Gal I, Shapira A, Shacham-Diamand Y, Dvir T, Engineered hybrid cardiac patches with multifunctional electronics for online monitoring and regulation of tissue function. Nat. Mater 15, 679–685 (2016). [PubMed: 26974408]

34. Martins AM, Eng G, Caridade SG, Mano JF, Reis RL, Vunjak-Novakovic G, Electrically conductive chitosan/carbon scaffolds for cardiac tissue engineering. Biomacromolecules 15, 635–643 (2014). [PubMed: 24417502]

35. Tang J, Wang J, Huang K, Ye Y, Su T, Qiao L, Hensley MT, Caranasos TG, Zhang J, Gu Z, Cheng K, Cardiac cell–integrated microneedle patch for treating myocardial infarction. Sci. Adv 4, eaat9365 (2018). [PubMed: 30498778]

36. Gaetani R, Feyen DAM, Verhage V, Slaats R, Messina E, Christman KL, Giacomello A, Doevendans PAFM, Sluijter JPG, Epicardial application of cardiac progenitor cells in a 3D-printed gelatin/hyaluronic acid patch preserves cardiac function after myocardial infarction. Biomaterials 61, 339–348 (2015). [PubMed: 26043062]

37. Tang J, Cui X, Caranasos TG, Hensley MT, Vandergriff AC, Hartanto Y, Shen D, Zhang H, Zhang J, Cheng K, Heart repair using nanogel-encapsulated human cardiac stem cells in mice and pigs with myocardial infarction. ACS Nano 11, 9738–9749 (2017). [PubMed: 28929735]

38. Freytes DO, Vunjak-Novakovic G, O'Neill J, Biomaterials derived from tissue extracellular matrix. US Patent App 15, 237 (2018).

39. Bassat E, Mutlak YE, Genzelinakh A, Shadrin IY, Umansky BK, Yifa O, Kain D, Rajchman D, Leach J, Bassat DR, Udi Y, Sarig R, Sagi I, Martin JF, Bursac N, Cohen S, Tzahor E, The extracellular matrix protein agrin promotes heart regeneration in mice. Nature 547, 179–184 (2017). [PubMed: 28581497]

40. Tang J, Shen D, Caranasos TG, Wang Z, Vandergriff AC, Allen TA, Hensley MT, Dinh P-U, Cores J, Li T-S, Zhang J, Kan Q, Cheng K, Therapeutic microparticles functionalized with biomimetic cardiac stem cell membranes and secretome. Nat. Commun 8, 13724 (2017). [PubMed: 28045024]

41. Luo L, Tang J, Nishi K, Yan C, Dinh P-U, Cores J, Kudo T, Zhang J, Li T-S, Cheng K, Fabrication of synthetic mesenchymal stem cells for the treatment of acute myocardial infarction in mice. Circ. Res 120, 1768–1775 (2017). [PubMed: 28298296]

42. Freytes DO, O'Neill JD, Duan-Arnold Y, Wrona EA, Vunjak-Novakovic G, Natural cardiac extracellular matrix hydrogels for cultivation of human stem cell-derived cardiomyocytes. Methods Mol. Biol 1181, 69–81 (2014). [PubMed: 25070328]

43. Kindi AA, Ge Y, Shum-Tim D, Chiu RC-J, Cellular cardiomyoplasty: Routes of cell delivery and retention. Front. Biosci 1, 2421–2434 (2008).

44. Sarig U, Sarig H, de-Berardinis E, Chaw S-Y, Nguyen EBV, Ramanujam VS, Thang VD, Al-Haddawi M, Liao S, Seliktar D, Kofidis T, Boey FYC, Venkatraman SS, Machluf M, Natural myocardial ECM patch drives cardiac progenitor based restoration even after scarring. Acta Biomater 44, 209–220 (2016). [PubMed: 27545814]

45. Koudstaal S, Jansen of Lorkeers SJ, Gho JMIH, van Hout GPJ, Jansen MS, Gründeman PF, Pasterkamp G, Doevendans PA, Hoefer IE, Chamuleau SAJ, Myocardial infarction and functional outcome assessment in pigs. J. Vis. Exp 25, e51269 (2014).

46. Tang J, Vandergriff A, Wang Z, Hensley MT, Cores J, Allen TA, Dinh P-U, Zhang J, Caranasos TG, Cheng K, A regenerative cardiac patch formed by spray painting of biomaterials onto the heart. Tissue Eng. Part C Methods 23, 146–155 (2017). [PubMed: 28068869]

47. Roura S, Soler-Botija C, Bagó JR, Llucià-Valldeperas A, Férnandez MA, Gálvez-Montón C, Prat-Vidal C, Perea-Gil I, Blanco J, Bayes-Genis A, Postinfarction functional recovery driven by a three-dimensional engineered fibrin patch composed of human umbilical cord blood-derived mesenchymal stem cells. Stem Cells Transl. Med 4, 956–966 (2015). [PubMed: 26106218]

48. Sharp TE, Schena GJ, Hobby AR, Starosta T, Berretta RM, Wallner M, Borghetti G, Gross P, Yu D, Johnson J, Feldsott E, Trappanese DM, Toib A, Rabinowitz JE, George JC, Kubo H, Mohsin S, Houser SR, Cortical bone stem cell therapy preserves cardiac structure and function after myocardial infarction. Circ. Res 121, 1263–1278 (2017). [PubMed: 28912121]

49. Hensley MT, de Andrade J, Keene B, Meurs K, Tang J, Wang Z, Caranasos TG, Piedrahita J, Li T-S, Cheng K, Cardiac regenerative potential of cardiosphere-derived cells from adult dog hearts. J. Cell. Mol. Med 19, 1805–1813 (2015). [PubMed: 25854418]

50. Ma Y, Wang B, Co-injection basic fibroblast growth factor for adipose derived stem cells transplantation: Improved cardiac remodelling and function of myocardial infarction. J. Am. Coll. Cardiol 63, S44 (2014).

51. Ye L, Chang Y-H, Xiong Q, Zhang P, Zhang L, Somasundaram P, Lepley M, Swingen C, Su L, Wendel JS, Guo J, Jang A, Rosenbush D, Greder L, Dutton JR, Zhang J, Kamp TJ, Kaufman DS, Ge Y, Zhang J, Cardiac repair in a porcine model of acute myocardial infarction with human

induced pluripotent stem cell-derived cardiovascular cell populations. Cell Stem Cell 15, 750–761 (2014). [PubMed: 25479750]

52. Jang J, Park H-J, Kim S-W, Kim H, Park JY, Na SJ, Kim HJ, Park MN, Choi SH, Park SH, Kim SW, Kwon S-M, Kim P-J, Cho D-W, 3D printed complex tissue construct using stem cell-laden decellularized extracellular matrix bioinks for cardiac repair. Biomaterials 112, 264–274 (2017). [PubMed: 27770630]

53. Park S-J, Kim RY, Park B-W, Lee S, Choi SW, Park J-H, Choi JJ, Kim S-W, Jang J, Cho D-W, Chung H-M, Moon S-H, Ban K, Park H-J, Dual stem cell therapy synergistically improves cardiac function and vascular regeneration following myocardial infarction. Nat. Commun 10, 3123 (2019). [PubMed: 31311935]

54. Shen D, Tang J, Hensley MT, Li T, Caranasos TG, Zhang T, Cheng K, Effects of matrix metalloproteinases on the performance of platelet fibrin gel spiked with cardiac stem cells in heart repair. Stem Cells Transl. Med 5, 793–803 (2016). [PubMed: 27112177]

55. Whyte W, Roche ET, Varela CE, Mendez K, Islam S, O'Neill H, Weafer F, Shirazi RN, Weaver JC, Vasilyev NV, McHugh PE, Murphy B, Duffy GP, Walsh CJ, Mooney DJ, Sustained release of targeted cardiac therapy with a replenishable implanted epicardial reservoir. Nat. Biomed. Eng 2, 416–428 (2018). [PubMed: 31011199]

56. Yuan X, Wei Y, Villasante A, Ng JJD, Arkonac DE, Chao P.-h. G., Vunjak-Novakovic G, Stem cell delivery in tissue-specific hydrogel enabled meniscal repair in an orthotopic rat model. Biomaterials 132, 59–71 (2017). [PubMed: 28407495]

57. Montgomery M, Ahadian S, Davenport Huyer L, Lo Rito M, Civitarese RA, Vanderlaan RD, Wu J, Reis LA, Momen A, Akbari S, Pahnke A, Li R-K, Caldarone CA, Radisic M, Flexible shape-memory scaffold for minimally invasive delivery of functional tissues. Nat. Mater 16, 1038–1046 (2017). [PubMed: 28805824]

58. Miragoli M, Ceriotti P, Iafisco M, Vacchiano M, Salvarani N, Alogna A, Carullo P, Ramirez-Rodríguez GB, Patrício T, Esposti LD, Rossi F, Ravanetti F, Pinelli S, Alinovi R, Erreni M, Rossi S, Condorelli G, Post H, Tampieri A, Catalucci D, Inhalation of peptide-loaded nanoparticles improves heart failure. Sci. Transl. Med 10, eaan6205 (2018). [PubMed: 29343624]

59. Ashammakhi N, Ahadian S, Darabi MA, Tahchi ME, Lee J, Suthiwanich K, Sheikhi A, Dokmeci MR, Oklu R, Khademhosseini A, Minimally invasive and regenerative therapeutics. Adv. Mater 31, 1804041 (2019).

60. Vagnozzi RJ, Maillet M, Sargent MA, Khalil H, Johansen AKZ, Schwanekamp JA, York AJ, Huang V, Nahrendorf M, Sadayappan S, Molkentin JD, An acute immune response underlies the benefit of cardiac stem cell therapy. Nature 577, 405–409 (2020). [PubMed: 31775156]

61. Zhu W, Zhao M, Mattapally S, Chen S, Zhang J, CCND2 overexpression enhances the regenerative potency of human induced pluripotent stem cell–derived cardiomyocytes: Remuscularization of injured ventricle. Circ. Res 122, 88–96 (2018). [PubMed: 29018036]

62. Ceholski DK, Turnbull IC, Pothula V, Lecce L, Jarrah AA, Kho C, Lee A, Hadri L, Costa KD, Hajjar RJ, Tarzami ST, CXCR4 and CXCR7 play distinct roles in cardiac lineage specification and pharmacologic β-adrenergic response. Stem Cell Res 23, 77–86 (2017). [PubMed: 28711757]

63. Bylund JB, Trinh LT, Awgulewitsch CP, Paik DT, Jetter C, Jha R, Zhang J, Nolan K, Xu C, Thompson TB, Kamp TJ, Hatzopoulos AK, Coordinated proliferation and differentiation of human-induced pluripotent stem cell-derived cardiac progenitor cells depend on bone morphogenetic protein signaling regulation by GREMLIN 2. Stem Cells Dev 26, 678–693 (2017). [PubMed: 28125926]

64. Su T, Huang K, Ma H, Liang H, Dinh P-U, Chen J, Shen D, Allen TA, Qiao L, Li Z, Hu S, Cores J, Frame BN, Young AT, Yin Q, Liu J, Qian L, Caranasos TG, Brudno Y, Ligler FS, Cheng K, Platelet-inspired nanocells for targeted heart repair after ischemia/reperfusion injury. Adv. Funct. Mater 29, 1803567 (2019). [PubMed: 32256277]

65. Vandergriff AC, Hensley MT, Cheng K, Isolation and cryopreservation of neonatal rat cardiomyocytes. J. Vis. Exp 9, e52726 (2015).

66. Cheng K, Malliaras K, Smith RR, Shen D, Sun B, Blusztajn A, Xie Y, Ibrahim A, Aminzadeh MA, Liu W, Li T-S, De Robertis MA, Marban L, Czer LSC, Trento A, Marbán E, Human cardiosphere-derived cells from advanced heart failure patients exhibit augmented functional potency in myocardial repair. JACC Heart Fail 2, 49–61 (2014). [PubMed: 24511463]

67. Drowley L, Koonce C, Peel S, Jonebring A, Plowright AT, Kattman SJ, Andersson H, Anson B, Swanson BJ, Wang Q-D, Brolen G, Human induced pluripotent stem cell-derived cardiac progenitor cells in phenotypic screening: A transforming growth factor-β type 1 receptor kinase inhibitor induces efficient cardiac differentiation. Stem Cells Transl. Med 5, 164–174 (2016). [PubMed: 26683871]

68. Sengupta P, The laboratory rat: Relating its age with human's. Int. J. Prev. Med 4, 624–630 (2013). [PubMed: 23930179]

69. Lang RM, Badano LP, Mor-Avi V, Afilalo J, Armstrong A, Ernande L, Flachskampf FA, Foster E, Goldstein SA, Kuznetsova T, Lancellotti P, Muraru D, Picard MH, Rietzschel ER, Rudski L, Spencer KT, Tsang W, Voigt J-U, Recommendations for cardiac chamber quantification by echocardiography in adults: An update from the American society of echocardiography and the European association of cardiovascular imaging. Eur. Heart J. Cardiovasc. Imaging 16, 233–270 (2015). [PubMed: 25712077]
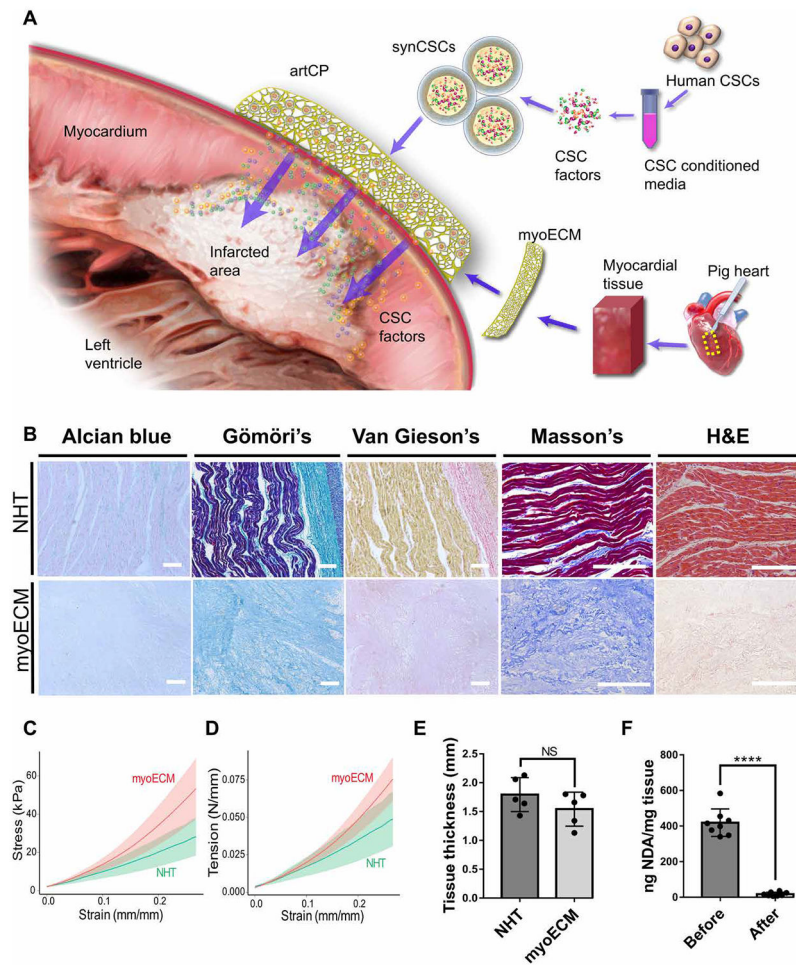
Fig. 1. Histological and mechanical comparison of decellularized myoECM and NHT.
(**A**) Schematic showing fabrication of artCP. (**B**) Histological comparison of NHT (top) and decellularized myoECM (bottom) including Alcian blue, Gormori's Blue, Van Gieson's, Masson's trichrome, and H&E staining. Scale bars, 200 μm. (**C** and **D**) Uniaxial testing on NHT and myoECM ($n = 5$). (C) Plots of tension versus strain. (D) Plots of stress versus strain. (**E**) Thickness comparison of NHT and myoECM samples for uniaxial testing. (**F**) DNA quantification before and after myoECM decellularization ($n = 8$). All data are means ± SD. Comparisons between two groups were performed using two-tailed unpaired Student's t test. NS indicates $P > 0.05$. ****$P < 0.0001$.
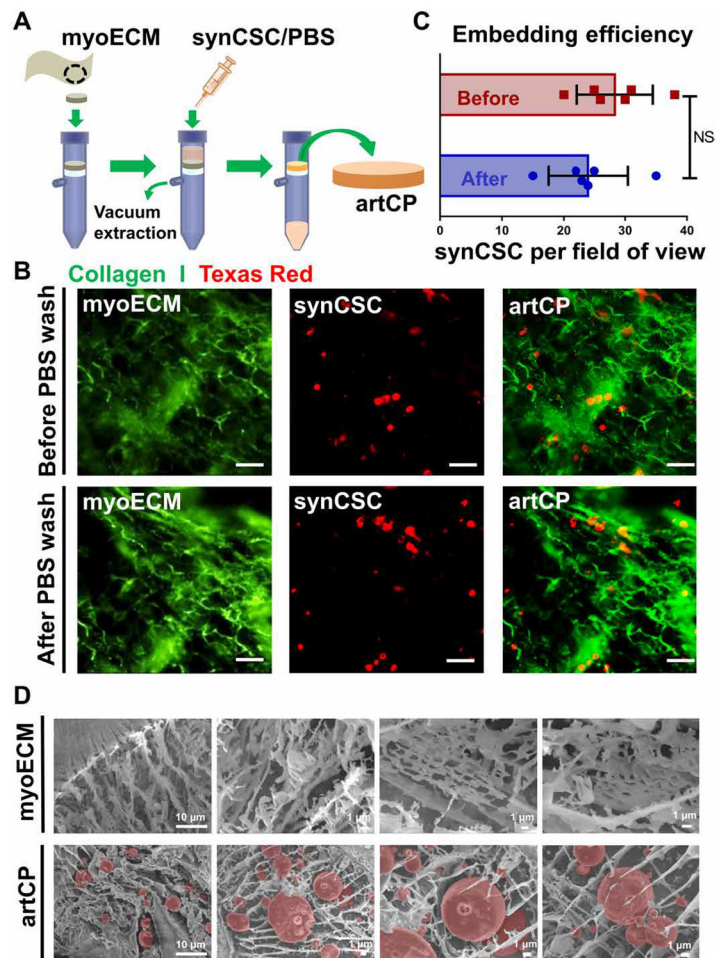
Fig. 2. Generation of artCP by embedding synCSCs into myoECM via vacuum filtration.
(**A**) Schematic showing the vacuum filtration method. (**B**) Representative fluorescence images showing artCPs before and after PBS wash. synCSCs (red) were prelabeled with Texas Red succinimidyl ester, and myoECM (green) was prelabeled with anti–collagen I and FITC-conjugated secondary antibodies. Scale bars, 25 μm. (**C**) Quantitation of embedded synCSCs before and after wash as in (B) ($n = 6$). All data are means ± SD. Comparisons between two groups were performed using two-tailed unpaired Student's t test. NS indicates $P > 0.05$. (**D**) Representative SEM images showing the cross-sectional view of myoECM and artCP. synCSCs are pseudocolored red.
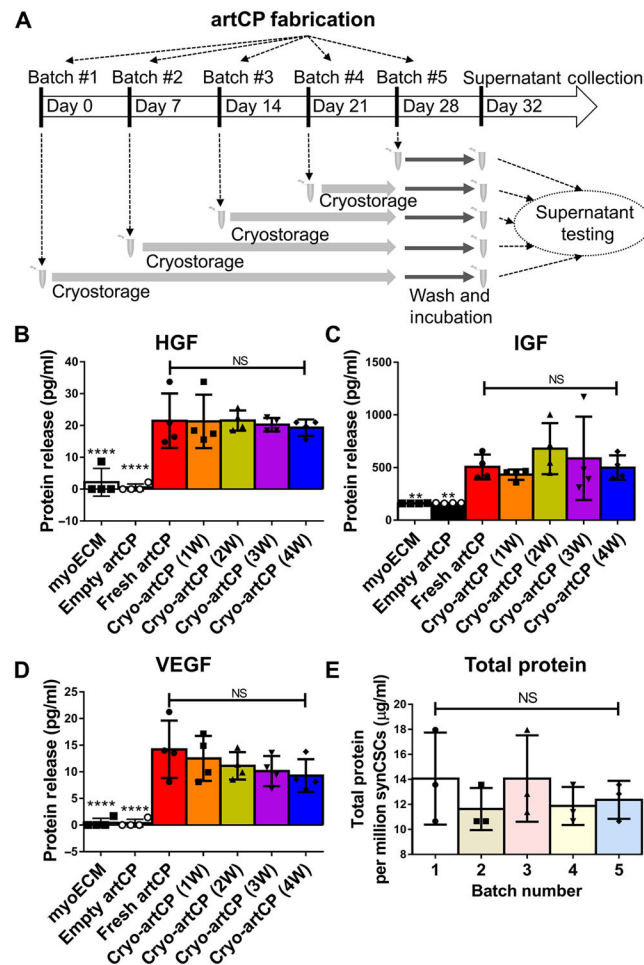
Fig. 3. Cryostability of artCPs.
(**A**) Schematic of the study design. (**B**) Hepatocyte growth factor (HGF), (**C**) insulin-like growth factor (IGF), and (**D**) vascular endothelial growth factor (VEGF) analyzed by ELISA ($n = 4$). myoECM and empty-artCP (myoECM embedded with empty-synCSCs) were used as controls. W, week. (**E**) Total protein amounts in different synCSC batches measured by the BCA Protein Assay Kit ($n = 3$). All data are means ± SD. Comparisons among groups were performed using one-way ANOVA followed by post hoc Bonferroni test. NS indicates $P > 0.05$. **$P < 0.01$ and ****$P < 0.0001$.
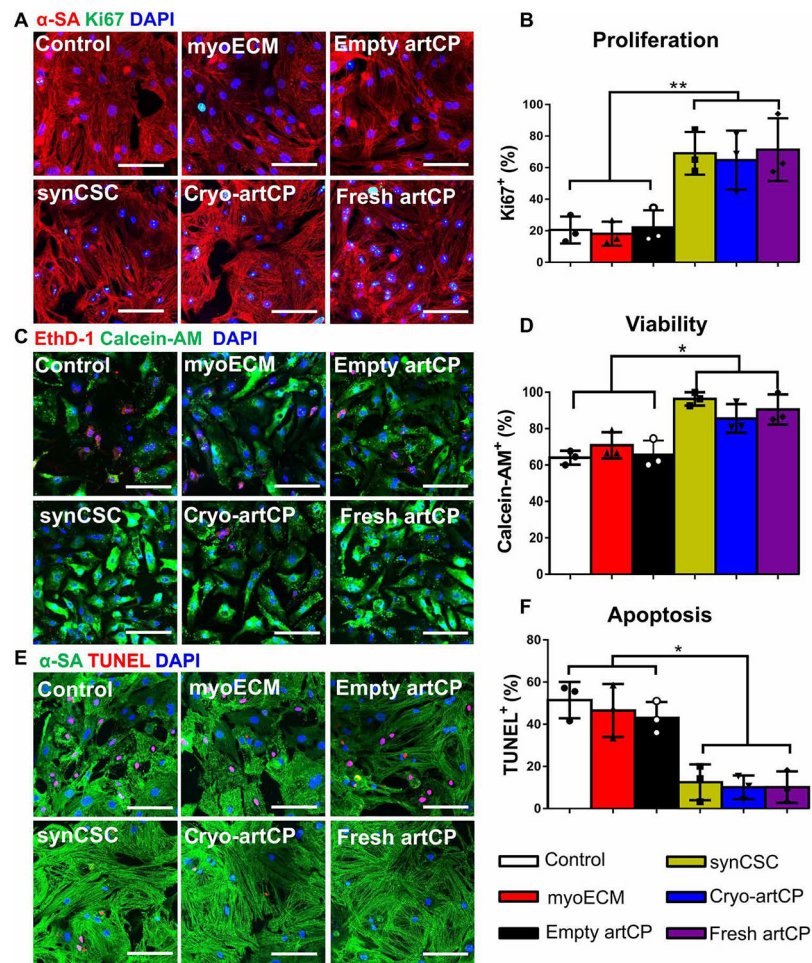
Fig. 4. Effects of artCP on cardiomyocytes in vitro.
(**A**) Representative fluorescence micrographs showing Ki67$^+$ expression (green) in NRCMs. Scale bars, 50 μm. α-SA, sarcomeric α-actinin. (**B**) Quantitation of Ki67$^+$ cells in (A) ($n =$ 3). (**C**) Representative fluorescence micrographs of LIVE/DEAD assay to determine the viability of NRCMs. Scale bars, 50 μm. (**D**) NRCM viability measured from (C) using ImageJ software ($n = 3$). (**E**) Representative fluorescence micrographs of cell apoptosis detected by terminal deoxynucleotidyl transferase–mediated deoxyuridine triphosphate nick end labeling (TUNEL) expression (red). Scale bars, 50 μm. (**F**) TUNEL$^+$ NRCM percentage determined from (E) using ImageJ software ($n = 3$). All data are means ± SD. Comparisons among groups were performed using one-way ANOVA followed by post hoc Bonferroni test. The comparisons between samples are indicated by lines, and the statistical significance is indicated by asterisks above the lines. *$P < 0.05$ and **$P < 0.01$.

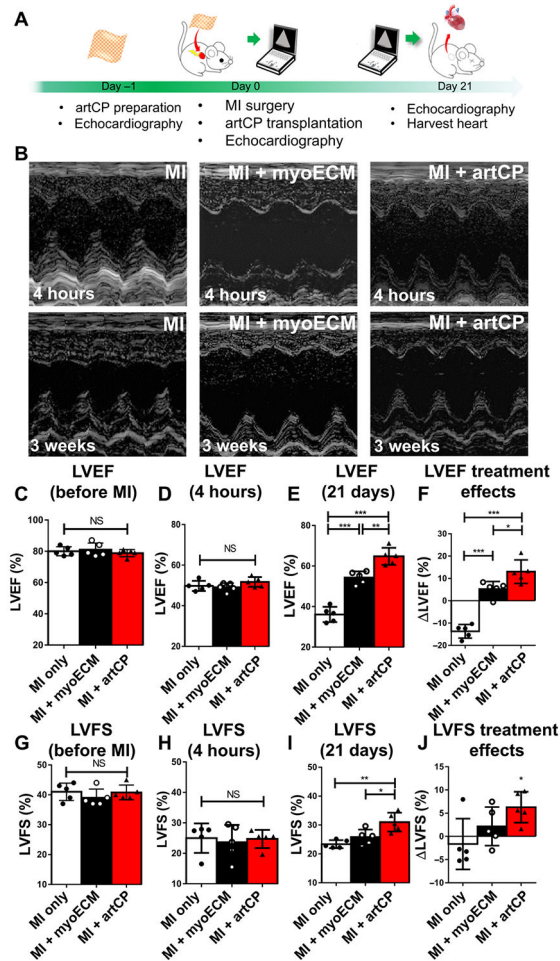**Fig. 5. Transplantation of artCPs in rats with MI.**
(**A**) Schematic showing the study design. Cardiac function was assessed before MI, 4 hours after MI (baseline), and 21 days after MI (end point). (**B**) Representative M-mode echocardiography images at baseline and end point taken from one animal in each group. LVEF was analyzed before MI (**C**), 4 hours after MI (**D**), and 21 days after MI (**E**). Treatment effects were determined as the change in LVEF from 4 hours after MI to 21 days after MI (**F**). $n = 5$ in each group. LVFS was also analyzed before MI (**G**), 4 hours after MI (**H**), and 21 days after MI (**I**), and treatment effects were calculated as the change in LVFS from 4 hours after MI to 21 days after MI (**J**). $n = 5$ in each group. All data are means ± SD. Comparisons among groups were performed using one-way ANOVA followed by post hoc Bonferroni test. The comparisons between samples are indicated by lines, and the statistical significance is indicated by asterisks above the lines. NS indicates $P > 0.05$. *$P < 0.05$, **$P < 0.01$, and ***$P < 0.001$.
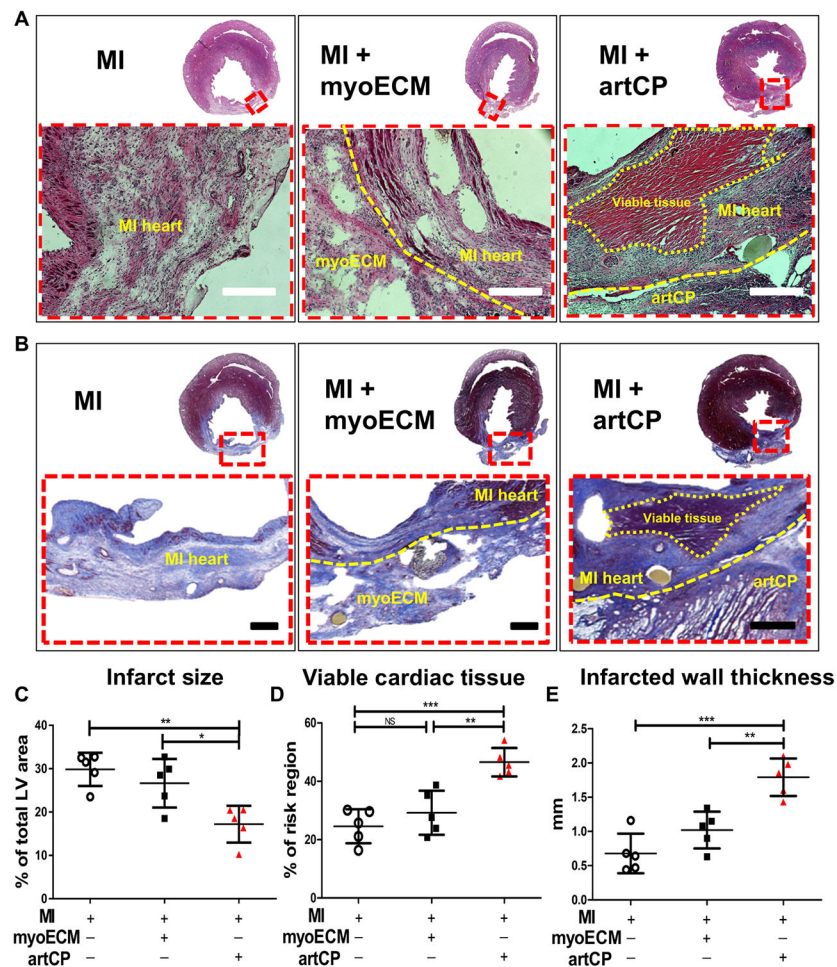
Fig. 6. Rat cardiac morphometry assessed through H&E and Masson's trichrome staining.
(**A**) H&E staining was performed on 10-µm cryosections of rat hearts 21 days after MI. Insets outlined by red dashed boxes are shown at higher magnification in the bottom row. Yellow dashed lines indicate the location of myoECM and infarcted tissue (middle) or viable tissue, infarcted tissue, and artCP (right). Scale bars, 250 µm. (**B**) Masson's trichrome staining performed on 5-µm cryosections. Insets outlined by red dashed boxes are shown at higher magnification in the bottom row. Yellow dashed lines indicate the location of myoECM and infarcted tissue (middle) or viable tissue, infarcted tissue, and artCP (right). Scale bars, 500 µm. Morphometric parameters including infarct size (**C**), the percentage of viable myocardium at risk area (**D**), and infarct wall thickness (**E**) were measured from the Masson's trichrome–stained slides via NIH ImageJ software. $n = 5$ in each group. All data are means ± SD. Comparisons among groups were performed using one-way ANOVA followed by post hoc Bonferroni test. The comparisons between samples are indicated by lines, and the statistical significance is indicated by asterisks above the lines. NS indicates $P > 0.05$. *$P < 0.05$, **$P < 0.01$, and ***$P < 0.001$.
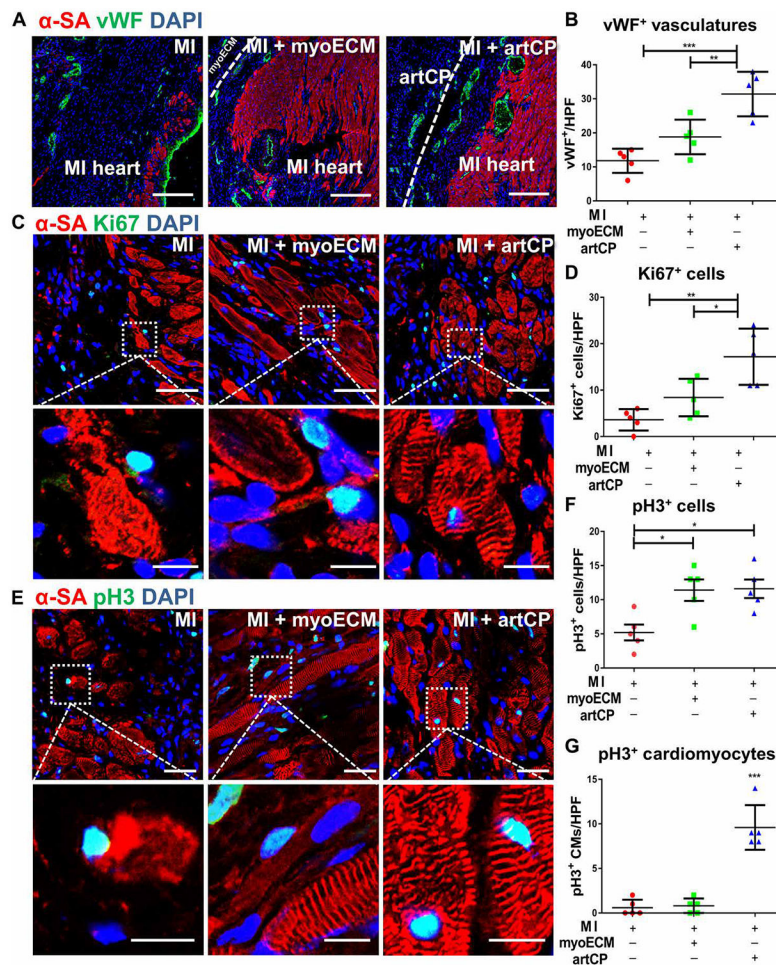
Fig. 7. IHC of rat cardiac tissue to explore the potential therapeutic mechanism of artCP.
(**A**) Endothelial cell marker von Willebrand factor (vWF) (green) was detected at day 21 in the heart-infarcted area that interfaced with transplanted artCP or myoECM. Scale bars, 200 μm. (**B**) The pooled data of vWF$^+$ signal per high-power field (HPF) assessed by ImageJ software ($n = 5$). (**C**) Ki67$^+$ expression (green) detected on the infarct periphery. Scale bars, 50 μm. Scale bars (zoomed snapshot), 10 μm. Insets are outlined by dashed white lines shown at higher magnification in the lower row. (**D**) Ki67$^+$ cells per HPF assessed by ImageJ software ($n = 5$). (**E**) Phosphorylated histone H3 (pH3$^+$) expression (green). Scale bars, 25 μm. Insets are outlined by dashed white lines shown at higher magnification in the lower row. Scale bars (higher magnification snapshots), 10 μm. (**F**) pH3$^+$ cells and (**G**) pH3$^+$ cardiomyocytes (nuclei inside of α-SA$^+$ cells that overlaid with pH3$^+$ signals) per HPF as assessed using ImageJ software ($n = 5$). CMs, cardiomyocytes. All data are means ± SD. Comparisons among groups were performed using one-way ANOVA followed by post hoc Bonferroni test. The comparisons between samples are indicated by lines, and the statistical significance is indicated by asterisks above the lines. *$P < 0.05$, **$P < 0.01$, and ***$P < 0.001$.
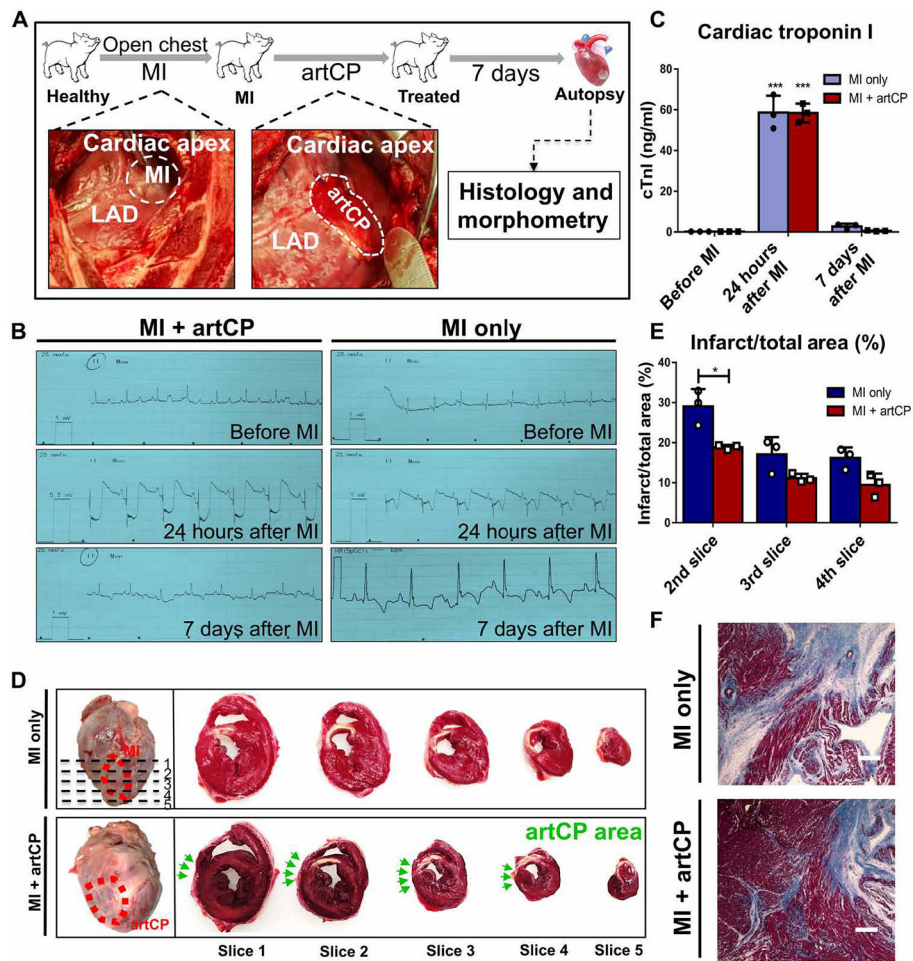
Fig. 8. Transplantation of artCP to porcine MI models.
(**A**) Schematic showing the study design. The representative pictures show the porcine MI model creation via LAD ligation (left) and artCP transplantation (right). (**B**) Electrocardiogram (ECG) was collected before MI and 24 hours and 7 days after MI. MI was indicated by ST segment elevation. (**C**) Serum cardiac troponin I (cTnI) was measured before MI and 24 hours and 7 days after MI in each group of animals ($n = 3$). (**D**) Heart sectioning for gross assessment of infarct size. The top left image (MI control) shows the area of infarction due to successful MI creation (red dashed circle) and five sections (1 cm in thickness; dashed line) cut from apex to level of ligation. The bottom left image shows the artCP transplanted area (red dashed circle). The images on the right show the TTC staining of five heart sections from one heart in the MI-only group (top) and the artCP-treated group (bottom). The white area in the TTC-stained heart sections indicates infarction. The position of artCP was indicated with green arrows. (**E**) Infarction area percentage measured in heart slices 2, 3, and 4 using ImageJ software ($n = 3$). All data are means ± SD. Comparisons among groups were performed using one-way ANOVA followed by post hoc Bonferroni test. The comparisons between samples are indicated by lines, and the statistical significance is indicated by asterisks above the lines. $*P < 0.05$ and $***P < 0.001$. (**F**) Masson's

trichrome staining of the infarct periphery performed to detect the myocardium integrity. Scale bars, 400 μm.